Dalton Transactions

PAPER

Check for updates

Ultrabroadband red luminescence of Mn^{4+} in MgAl$_2$O$_4$ peaking at 651 nm†

Haipeng Ji, [ID] [a] Xinghui Hou, [ID] [a] Maxim S. Molokeev, [ID] [b,c] Jumpei Ueda, [ID] [d] Setsuhisa Tanabe, [ID] [d] Mikhail G. Brik, [ID] [e,f] Zongtao Zhang, [ID] [a] Yu Wang [ID] *[a] and Deliang Chen [ID] *[a,g]

Blue light pumped red luminescence with broadband and high photon-energy emission is highly desired for phosphor-converted white light-emitting diodes (pc-wLEDs), to achieve a high color rendering index and high luminous efficacy. Mn^{4+}-doped red-emitting phosphors generally exhibit sharp vibronic emissions associated with the parity- and spin-forbidden $^2E_g \rightarrow {}^4A_{2g}$ transitions. In this paper, two abnormal luminescence behaviors were observed for Mn^{4+} in the MgAl$_2$O$_4$:Mn^{4+} spinel phosphor with a short wavelength emission band peaking at 651 nm. Firstly, the Mn^{4+} $^2E_g \rightarrow {}^4A_{2g}$ transition exhibits ultrabroadband luminescence in MgAl$_2$O$_4$ and the large full-width at half-maximum (FWHM) is dependent both on the calcination temperature and on the partial substitution of Al^{3+} with Ga^{3+}. Secondly, the thermal quenching behavior of the Mn^{4+} $^2E_g \rightarrow {}^4A_{2g}$ luminescence in MgAl$_2$O$_4$ shows a dependence on its thermal treatment and preparation method. The Rietveld refinement and Raman results demonstrate that the variation in the FWHM of the luminescence spectra is a sum effect of structural ordering (*i.e.*, isotropic displacement decrease of constituent atoms) and the Mg ↔ Al anti-site disorder. A model for the observed varying thermal quenching of luminescence was tentatively proposed. The intrinsic thermal quenching temperature of Mn^{4+} luminescence in MgAl$_2$O$_4$ was found to be 390−400 K using the samples prepared by the co-precipitation and molten salt methods. The present work gives a novel perspective to understand the luminescence spectra of Mn^{4+} $^2E_g \rightarrow {}^4A_{2g}$ transition.

1 Introduction

Dominant phosphor-converted white light-emitting diodes (pc-wLEDs), formed by combining blue-emitting LEDs and yellow-emitting phosphors (such as Y$_3$Al$_5$O$_{12}$:Ce^{3+}), generate cool white light with a relatively high correlated color temperature (CCT >4500 K) and a low color rendering index (CRI; $R_a <$ 80) due to the lack of the red component.[1] In recent decades, 3.5MgO·0.5MgF$_2$·GeO$_2$:Mn^{4+} has been commercially used as a

red phosphor in fluorescent lamps. Since the commercialization of Mn^{4+} activated fluoride phosphors (typically K$_2$SiF$_6$:Mn^{4+}) for blue LED pumped white lighting,[2] Mn^{4+} has been intensively investigated as a blue-to-red converting ion for LED phosphors. The spin-allowed Mn^{4+} $^4A_{2g} \rightarrow {}^4T_{2g}$ transition can be excited by a blue LED avoiding the cascade reabsorption of yellow light from the yellow-emitting phosphor; furthermore, manganese is more abundant than the rare earth elements (Eu^{2+}, Ce^{3+}, *etc.*), which is helpful to lower the production cost of red phosphors.[3]

The Mn^{4+} ion with the 3d^3 electronic configuration prefers to get stabilized in octahedral symmetry with the three d-electrons occupying the three low-lying t$_{2g}$ orbitals split by the octahedral field. The MgAl$_2$O$_4$ spinel is a typical host containing [AlO$_6$] octahedra, and Mg^{2+}/Al^{3+} occupies the tetrahedral/octahedral sites, respectively. MgAl$_2$O$_4$ can perfectly accommodate Mn^{4+}, because the effective ionic radius of the 6-fold coordinated Al^{3+} (r = 0.535 Å) is close to that of Mn^{4+} (r = 0.530 Å). MgAl$_2$O$_4$ also possesses a high Debye temperature (776 K) for its single crystal,[4] suggesting a quite rigid crystal lattice. Although a number of aluminates have been studied as hosts for Mn^{4+} such as SrAl$_{12}$O$_{19}$, Sr$_4$Al$_{14}$O$_{25}$, SrAl$_4$O$_7$, *etc.*, our as-prepared MgAl$_2$O$_4$:Mn^{4+} shows luminescence with a very

[a]School of Materials Science and Engineering, Zhengzhou University, Zhengzhou 450001, China. E-mail: wangyu@zzu.edu.cn, dlchen@zzu.edu.cn

[b]Laboratory of Crystal Physics, Kirensky Institute of Physics, Federal Research Center KSC SB RAS, Krasnoyarsk 660036, Russia

[c]Siberian Federal University, Krasnoyarsk 660041, Russia

[d]Graduate School of Human and Environmental Studies, Kyoto University, Kyoto 606-8501, Japan

[e]CQUPT-BUL Innovation Institute & College of Sciences, Chongqing University of Posts and Telecommunications, Chongqing 400065, China

[f]Institute of Physics, University of Tartu, Tartu 50411, Estonia

[g]School of Materials Science and Engineering, Dongguan University of Technology, Dongguan 523808, China

†Electronic supplementary information (ESI) available. See DOI: 10.1039/D0DT00931H

short wavelength peaking at 651 nm, which is the shortest peak wavelength of the Mn^{4+} $^2E_g \rightarrow$ $^4A_{2g}$ transition that has ever been observed in Mn^{4+}-doped aluminates. Table 1 lists a number of Mn^{4+}-doped aluminate phosphors; the shortest emission wavelength of Mn^{4+} that has been achieved is found to be 652 nm in either $Sr_4Al_{14}O_{25}$ or $Sr_2Al_6O_{11}$. Furthermore, typical Mn^{4+}-doped red-emitting phosphors, for example, the K_2SiF_6:Mn^{4+} phosphor, usually exhibit sharp vibronic emissions arising from the intraconfigurational parity- and spin-forbidden $^2E_g \rightarrow$ $^4A_{2g}$ transitions. However, the full-width at half-maximum (FWHM) of the as-prepared $MgAl_2O_4$:Mn^{4+} is relatively quite large. As indicated by the Tanabe–Sugano diagram for a d^3 ion,[5] the luminescence would be from the spin-allowed $^4T_{2g} \rightarrow$ $^4A_{2g}$ transition exhibiting broadband emission when the ion experiences a weak crystal field, while it will exhibit sharp emission peaks in a strong crystal field arising from the spin-forbidden $^2E_g \rightarrow$ $^4A_{2g}$ transition. Mn^{4+} tends to experience a large crystal field strength due to a high effective positive charge, and only transition from the ^2E_g level is expected. Thus, the origin of the broadband emission observed for $MgAl_2O_4$:Mn^{4+} remains to be verified.

In this paper, we used a co-precipitation method to prepare the $MgAl_2O_4$:Mn^{4+} phosphors by treating the precursors at 700, 1000, or 1300 °C to control their anti-site disorder degree and investigate its effect on the luminescence properties. We report the findings on the correlation between the varying FWHMs and the anti-site defect as well as the isotropic displacement of constituent atoms in $MgAl_2O_4$:Mn^{4+}. Moreover, the thermal quenching behaviors of the $MgAl_2O_4$:Mn^{4+} phosphors were systemically investigated, which were found to be abnormally dependent on the thermal treatment and methods of preparation. These findings on the origin of the varying FWHM and thermal quenching behavior are expected to inspire the development of new Mn^{4+}-activated broadband and thermally robust red-emitting phosphors for blue LED pumped white lighting.

2 Experimental and computational methods

2.1 Preparation

The phosphors with a nominal composition of $MgAl_{2-x}Mn_xO_4$ ($x = 0.002$) were synthesized by a co-precipitation method.[29] $MgCl_2 \cdot 6H_2O$ (A.R., Sinopharm, China), $Al(NO_3)_3 \cdot 9H_2O$ (A.R., Sinopharm, China) and $Mn(NO_3)_2$ (50 wt% solution, Aladdin, China) were used as raw chemicals, and ammonia water (NH_4OH 28%, Sinopharm, China) was used as the precipitating agent. A metal nitrate solution, which contains 20 mmol of Al^{3+}, 10 mmol of Mg^{2+} and $10x$ mmol of Mn^{2+}, was prepared by dissolving the raw nitrates in 50 ml of deionized water. Then, the metal nitrate solution was added dropwise into 50 mL of ammonia water under magnetic stirring. White precipitates appeared instantly upon mixing. The pH of the resultant suspension was around 10. Next, the suspension was aged at 75 °C for 1 h in a water bath. After aging, the solid in the suspension was concentrated by centrifugation at 5000 rpm for 5 min and then dried at 110 °C for 12 h. The obtained precursor showed a light pink color and was quite glutinous. Thus, without grinding, the precursor was heated at 450 °C for 3 h (at this temperature, nucleation of $MgAl_2O_4$ started[30]), then thoroughly ground, and finally sintered for 3 h at 700 °C, 1000 °C, or 1300 °C, respectively. All heat treatments were conducted in air. Fig. 1a illustrates the above procedure.

Table 1 Mn^{4+}-doped aluminate phosphors and the corresponding peaking emission

No.	Phosphor	Peaking wavelength
1	$Sr_4Al_{14}O_{25}$:Mn^{4+}	652 nm (ref. 6 and 7)
2	$Sr_2Al_6O_{11}$:Mn^{4+}	652 nm (ref. 8)
3	$SrAl_{12}O_{19}$:Mn^{4+}	655 nm (ref. 9)
4	$CaMg_2Al_{16}O_{27}$:Mn^{4+}	655 nm (ref. 10)
5	$SrAl_4O_7$:Mn^{4+} ^{a}	656 nm (ref. 11)
6	$CaAl_4O_7$:Mn^{4+} ^{a}	656 nm (ref. 12)
7	$Sr_2MgAl_{22}O_{36}$:Mn^{4+}	658 nm (ref. 13)
8	$CaAl_{12}O_{19}$:Mn^{4+}	658 nm (ref. 14)
9	$SrMgAl_{10}O_{17}$:Mn^{4+}	660 nm (ref. 15)
10	$BaMgAl_{10}O_{17}$:Mn^{4+}	660 nm (ref. 16)
11	$ZnAl_2O_4$:Mn^{4+}	666 nm (ref. 17)
12	α-$LiAlO_2$:Mn^{4+}	670 nm (ref. 18)
13	$Y_3Al_5O_{12}$:Mn^{4+}	670 nm (ref. 19)
14	$CaY_2Al_4SiO_{12}$:Mn^{4+}	674 nm (ref. 20)
15	Al_2O_3:Mn^{4+}	676 nm (ref. 21)
16	$YAlO_3$:Mn^{4+}	697 nm (ref. 22)
17	$GdAlO_3$:Mn^{4+}	698 nm (ref. 23)
18	$CaYAlO_4$:Mn^{4+}	710 nm (ref. 24)
19	$LaAlO_3$:Mn^{4+}	712 nm (ref. 25)
20	$LiAl_5O_8$:Mn^{4+}	714 nm (ref. 26)
21	$Ca_{14}Al_{10}Zn_6O_{35}$:Mn^{4+}	715 nm (ref. 27)
22	$SrLaAlO_4$:Mn^{4+}	715 nm (ref. 28)

^{a} These compounds do not consist of octahedral coordination.

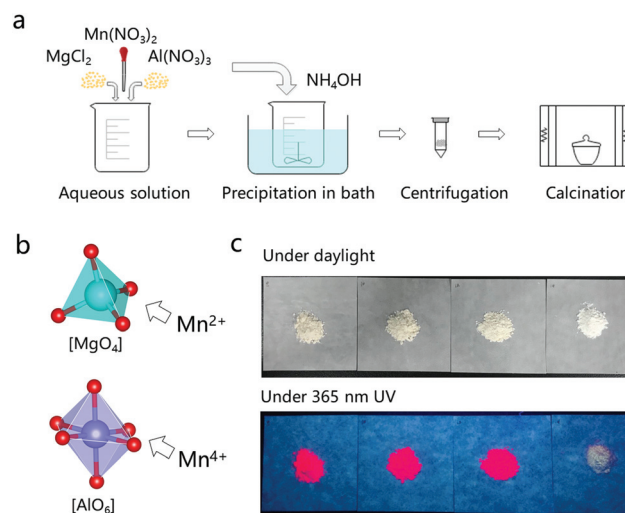**Fig. 1** (a) Synthesis flow chart, (b) the [MgO_4] tetrahedron and [AlO_6] octahedron in $MgAl_2O_4$ which can accommodate manganese as Mn^{2+} or Mn^{4+}, (c) digital image of the $MgAl_2O_4$:Mn phosphors under daylight or 365 nm UV irradiation (from left to right: the calcination schedule is 700 °C × 3 h, 1000 °C × 3 h, 1300 °C × 3 h, and 1400 °C × 12 h, respectively). The difference in color is related to the different absorption properties of the phosphors, which originate from the distribution of $Mn^{4+/2+}$ in [AlO_6] or [MgO_4].

Furthermore, to chemically introduce the anti-site disorder, Al^{3+} in $MgAl_2O_4$ was partially substituted by Ga^{3+}. The solid solution phosphors with nominal compositions of $MgAl_{2-y}Ga_yO_4$:0.002Mn^{4+} (y = 0, 0.5, 1.0) were prepared by a high-temperature solid state reaction. Stoichiometric ratios of MgO, Al_2O_3, Ga_2O_3 and $MnCO_3$ chemicals (all A.R. grade) were weighed and mixed thoroughly in an agate motor by hand, then preheated at 450 °C for 3 h and then finally heated at 1550 °C for 6 h. The products were pulverized into fine powder prior to optical measurements.

2.2 Characterization

X-ray diffraction (XRD) patterns were collected on an X-ray diffractometer (DX-2700BH, DanDong Haoyuan Instrument Co. Ltd, Liaoning, China) using Cu-Kα radiation with an operating voltage and current of 40 kV and 30 mA, respectively. The XRD patterns for phase identification and for Rietveld refinement were collected in the 2θ range of 10–80° (step 0.02°, exposition time 0.2 s per step) and 10–120° (step 0.02°, exposition time 1.5 s per step), respectively. Rietveld refinements of the crystal structure were implemented using the TOPAS software.[31] Photoluminescence excitation (PLE) spectra were recorded using a spectrofluorometer (FluoroMax-4, Horiba Jobin Yvon, France). Temperature-dependent photoluminescence emission (PL) was measured in the temperature range of 100 K to 470 K using the setup as described previously,[32] which consists of a multichannel charge-coupled device (QE65Pro, Ocean Optics, USA) and a thermal stage (10033L, Linkham, UK); a 440 nm laser diode with a 550 nm short-cut filter was employed as the excitation source. The morphology was observed on a scanning electron microscope (SEM; TM3030Plus Tabletop, Hitachi, Japan). The powder sample was ultrasonically dispersed in ethanol to form a suspension which was dropped on a silicon plate. Raman spectra were collected on a LabRAM HR Evolution spectrometer (Horiba Jobin Yvon, France) at room temperature, using the 532 nm laser light as an excitation source.

2.3 Computational details

The energy levels of the Mn^{4+} ions in $MgAl_2O_4$ were theoretically calculated using the exchange charge model. The crystal structure data for $MgAl_2O_4$ were used to analyze the symmetry properties of the impurity ion site and generate a cluster consisting of 62 210 ions (this was needed to ensure the appropriate convergence of the crystal lattice sums needed for the calculations of the crystal field parameters). Details of the calculations and all relevant equations are provided in several related references (ref. 25,33–35). Briefly, we can mention that the coordinates of ions from the above-mentioned large cluster were used to calculate the parameters of the crystal field Hamiltonian acting upon the unfilled 3d electron shell of the Mn^{4+} ions. As the next step, the crystal field Hamiltonian was diagonalized in the basis set consisting of all wave functions of 8 LS terms of the Mn^{4+} ion. The eigenvalues of this Hamiltonian corresponded to the crystal field splitting of the free ion terms and were compared with the experimental excitation/emission spectra to verify the validity of the obtained results. Section 3.2 contains all calculated data and discussion of their relation to the experimentally determined optical properties of $MgAl_2O_4$:Mn^{4+}.

3 Results and discussion

3.1 Phase formation and the selective occupation of the manganese dopant

The structure of $MgAl_2O_4$ (ICSD 31373) comprises both [MgO_4] tetrahedra and [AlO_6] octahedra, which can accommodate manganese either as Mn^{2+} or Mn^{4+} (illustrated in Fig. 1b). Mn^{4+} with the $3d^3$ electronic configuration gets stabilized when doped into the [AlO_6] octahedron. As shown in Fig. S1,† these octahedra have an equal $d_{Al–O}$ bond length of 1.9259(9) Å, but the angles between the Al–O bonds can be divided into two sets of 96.06(7)° and 83.94(7)°. Thus, the point symmetry of the Al^{3+} site is lowered to C_{3i} from O_h (for an ideal octahedron). The samples calcined at 700, 1000 or 1300 °C for 3 h show the body color of light pink and emit red when irradiated at 365 nm, while the one calcined at higher temperature for longer duration (such as 1400 °C for 12 h) appears white and emits green under 365 nm irradiation (shown in Fig. 1c). This evidences that manganese was firstly doped into the six-fold coordinated Al^{3+} site as Mn^{4+}, and then, under higher temperature and longer duration conditions, it was found to occupy the four-fold coordinated Mg^{2+} site as Mn^{2+}. This result contributes new knowledge about the selective occupation of manganese in $MgAl_2O_4$, in addition to that revealed by Wakui et al.[36] (that is, excess MgO in starting materials favors the substitution of Mn^{4+} in the octahedral site, while deficient MgO leads to the substitution of Mn^{2+} in the tetrahedral site for $MgAl_2O_4$:Mn synthesized by solid state reaction at 1400–1600 °C for 5 h[36]). All samples were single spinel phases as indicated by XRD (shown in Fig. 2 and Fig. S2†). Several diffraction halos with quite low intensity were observed for the precursor heated at 450 °C. Then, crystalline $MgAl_2O_4$ was formed when heated at 700 °C. Intensities of the diffraction peaks got increased and the peaks became sharper along with the temperature rise. All diffraction peaks coincide with the reference ($MgAl_2O_4$, JCPDS no. 47-0254).

3.2 Temperature-induced inhomogeneous broadening of the luminescence spectra of $MgAl_2O_4$:Mn^{4+}

Fig. 3 shows the PLE/PL spectra of the $MgAl_2O_4$:Mn^{4+} phosphors prepared at 700–1300 °C (PL/PLE spectra of the phosphor synthesized at 1400 °C showing green emission from Mn^{2+} are provided in ESI Fig. S3†). The PLE spectra consist of two broad bands in the 250–350 nm and 400–500 nm ranges, originating from the $O^{2-} \rightarrow Mn^{4+}$ charge transfer (CT) transition and the spin-allowed $^4A_{2g} \rightarrow {}^4T_{1g}$ and $^4A_{2g} \rightarrow {}^4T_{2g}$ transitions. The PLE bands in the blue spectral range peak at 440 nm, suitable for blue LED pumping. The emissions peak at 651 nm caused by the ZPL emission and/or the associated phonon sidebands and show no clear fine structure. The PL
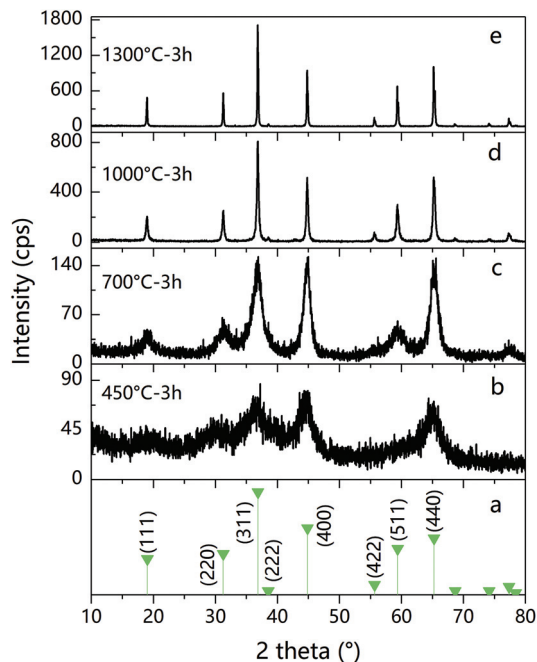
Fig. 2 XRD patterns of the phosphors calcined at 450 °C (b), 700 °C (c), 1000 °C (d), and 1300 °C (e) for 3 h. The standard pattern of MgAl$_2$O$_4$ (JCPDS no. 47-0254) was provided as reference (a).

the case of spin-allowed transition, we believe that the emitting level is ^2E_g instead of $^4T_{2g}$ since Mn^{4+} tends to experience a strong crystal field due to a higher positive charge than Cr^{3+}.[37]

Moreover, by comparing the PL spectra recorded at temperatures of 100 K and 293 K, the ZPL emission can be found to be around 651 nm (15 361 cm^{-1}) as the anti-Stokes emission (the higher energy side of ZPL emission) got enhanced at 293 K compared to that measured at 100 K. The [AlO$_6$] octahedron in MgAl$_2$O$_4$ exhibits a slight distortion caused by the O–Al–O bond angle variation (Fig. S1†), and such distortion could lead to the splitting of the emitting doublet state and the vibronic phonon sideband emissions as well as the mixing of the ^2E_g state with the $^4T_{2g}$ state. Thus, it is quite difficult to identify whether the strongest emission peak (651 nm) belongs to the ZPL or the phonon sideband emission, and the ZPL emission could be at a slightly shorter wavelength (for example, 650 nm). This demonstrated a quite high $^2E_g \rightarrow {}^4A_{2g}$ transition energy of Mn^{4+} among the so-far reported oxide hosts;[38] higher $^2E_g \rightarrow {}^4A_{2g}$ transition energy is only achieved in some germanates (such as Mg$_4$GeO$_6$ and Mg$_{14}$Ge$_5$O$_{24}$) and arsenates (such as Mg$_6$As$_2$O$_{11}$). Such high ZPL energy demonstrates the advantage of developing this spinel phosphor. The chromaticity of red fluorescence of MgAl$_2$O$_4$:Mn^{4+} is $x = 0.722$, $y = 0.278$ and is drawn in the CIE (Commission Internationale de l'Eclairage) diagram as shown in Fig. S4;† the chromaticity of 3.5MgO·0.5MgF$_2$·GeO$_2$:Mn^{4+} ($x = 0.711$, $y = 0.289$, measured using the commercial product of Kasei Optonix by Murata et al.[14]) is also given for comparison.
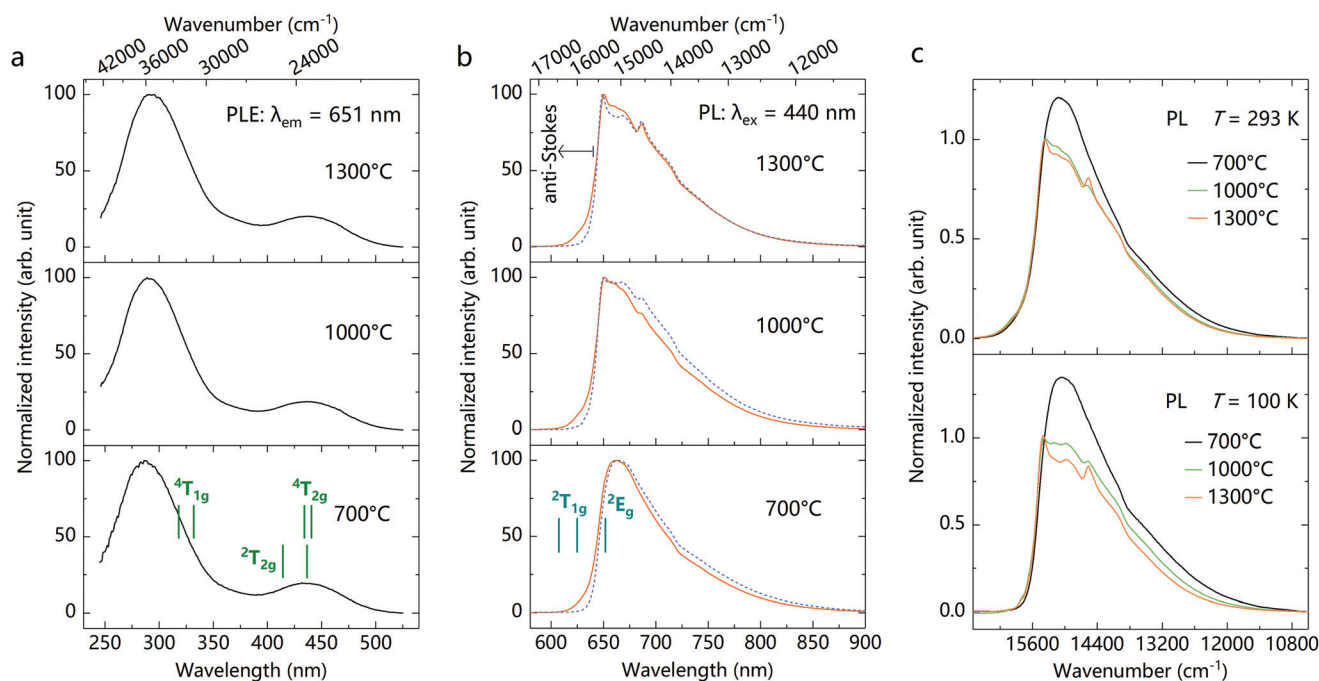
spectra exhibit a single asymmetric broad band, with intensity decreasing more steeply with increasing photon energy. Although the PL spectra are quite broad, which is similar to

Fig. 3 Normalized PLE (a) and PL (b) spectra of the MgAl$_2$O$_4$:Mn^{4+} phosphors heated at 700 °C, 1000 °C, or 1300 °C for 3 h, respectively. The PL spectra were comparatively recorded at T = 293 K (red) and 100 K (blue) in (b). (c) PL bands of the MgAl$_2$O$_4$:Mn^{4+} phosphors normalized at the emission at 651 nm (15 361 cm^{-1}).

The Mn^{4+} energy levels in $MgAl_2O_4$ were also calculated theoretically. A large cluster consisting of 62 210 ions was built up to ensure the appropriate convergence of the crystal lattice sums needed for calculation of the crystal field parameters. The trigonal symmetry of the Al site was confirmed by the structure of the crystal field Hamiltonian, in which only the following crystal field parameters were not zero (in cm^{-1}, Stevens normalization): $B_2^0 = 2488$, $B_4^0 = -4428$, $B_4^3 = 107\,938$. The Racah parameter values were (in cm^{-1}) $B = 800$ and $C = 3157$, respectively. The calculated Mn^{4+} energy levels (in cm^{-1}; only those energy levels which are relevant for the discussion of the spectroscopic measurements are given; the asterisk indicates the orbital doublet states) are as follows: $^4A_{2g}$ – 0; ^2E_g – 15 361*; $^2T_{1g}$ – 16 025* and 16 483; $^2T_{2g}$ – 22 924 and 24 121*; $^4T_{2g}$ – 22 718* and 23 058; $^4T_{1g}$ – 30 133 and 31 526*. The character of the orbital triplets splitting into a singlet and a doublet state is also in line with the trigonal symmetry of the Mn^{4+} position. Agreement with the experimental spectra is visualized in Fig. 3, wherein the calculated energy levels are shown by the vertical bars.

The PL bands of the phosphors heated at 1000 and 1300 °C with higher crystallinity consistently peak at 651 nm. However, there exists an obvious difference between these PL bands in the lower energy sides (the phonon sidebands), which thus induced varying FWHM (Full-Width at Half-Maximum) of the PL bands. The FWHM can be evaluated in two ways, either the value difference at the half-maximum or the value of the integrated area dividing the peak. Considering the asymmetric feature of the PL bands, we here evaluate the FWHMs using the second method. Fig. 3c shows the PL bands which were normalized at 651 nm. The estimated FWHMs using such normalized PL bands are 2093 cm^{-1} ($T = 293$ K)/2416 cm^{-1} ($T = 100$ K), 1811 cm^{-1} ($T = 293$ K)/1936 cm^{-1} ($T = 100$ K), and 1772 cm^{-1} ($T = 293$ K)/1733 cm^{-1} ($T = 100$ K), for the phosphors synthesized at 700 °C, 1000 °C, and 1300 °C, respectively. Increase in the heating temperature leads to a decrease in the FWHM of the PL bands. Such variation is not significant but reflects some interesting intrinsic change in factors affecting the Mn^{4+} $^2E_g \rightarrow {}^4A_{2g}$ transition.

Generally, the origin of the broad FWHM of the PL bands can be the inhomogeneous broadening effect, which is a well-known phenomenon observed in solid solution phosphors exhibiting d–f parity-allowed transition, for example, $Lu_3(Al_{2-x}Mg_x)$ $(Al_{3-x}Si_x)O_{12}:Ce^{3+}$ ($x = 0.5$–2.0),[39] $Y_xLu_{3-x}MgAl_3SiO_{12}:Ce^{3+}$ ($x = 0$–3)[40] and $M_3(PO_4)_2:Eu^{2+}$ (M = Ca, Sr, Ba)[41] phosphors. The inhomogeneous broadening of the PL bands is induced by a higher diversity of local coordination environments of the activator ions in solid-solution compositions. We presume that the FWHM deviation of the PL bands of $MgAl_2O_4:Mn^{4+}$ exhibiting the d–d parity-forbidden transition can be explained in the same way. The diversity of the local coordination environments can be induced in multiple ways,[42] for instance, the interstitial cation, the cation/anion vacancy, and the cation antisite-occupation, which finally lead to the first nearest coordination sphere (i.e., the MnO_6 octahedra) offsetting the average situation. Among them, the cation anti-site occupation

($Mg_{Mg}^\times + Al_{Al}^\times \rightarrow Al_{Mg}^\cdot + Mg_{Al}'$ in the Kröger–Vink notation) is known to occur in a synthetic spinel. As the concentration of Mg ↔ Al anti-site disorder is influenced by the thermal treatment of the spinel phosphor, it may be the origin of the observed inhomogeneous broadening. This anti-site disorder indicates the self-compensation of Mn_{Al}-substitution with Mg^{2+}. Because of the anti-site associated charge compensation, there is a range of distortions around the Mn^{4+} ions, which tend to obscure the fine-structure details of the zero-phonon $^2E_g \rightarrow {}^4A_{2g}$ transitions of the Mn^{4+} spectrum.[19] Meanwhile, the anti-site disorder could further lower the point symmetry of the Al^{3+} site, causing the splitting of the emitting doublet state.

We thus try to semi-quantitatively evaluate the anti-site disorder concentrations by checking the lattice dimension evolution via Rietveld refinement. Theoretically, if we replace Mg^{2+} in the tetrahedral 8a site by an x amount of Al^{3+}, the average ionic radii of the 8a site (IR_{8a}) become $x \times 0.39 + (1 - x) \times 0.57$ ($r_{Al^{3+},CN=4} = 0.39$ Å; $r_{Mg^{2+},CN=4} = 0.57$ Å) (CN: coordination number). Since the octahedral 16d site has a twice bigger multiplicity than the 8a site, the 16d site loses only $x/2$ Al^{3+}. Thus, the average ionic radii of the 16d site (IR_{16d}) become $(1 - x/2) \times 0.535 + (x/2) \times 0.72$ ($r_{Mg^{2+},CN=6} = 0.72$ Å, $r_{Al^{3+},CN=6} = 0.535$ Å). The variation of the lattice parameter with respect to the anti-site disorder in $(Mg_{1-i}Al_i)[Mg_iAl_{2-i}]$ O_4 has been shown to be small; a change of 0.1 in i modifies the lattice parameter by just 0.0025 Å.[43] Thus, the cell volume (V) change is chosen to reveal the anti-site disorder. V should be proportional to $1/3(IR_{8a}) + 2/3(IR_{16d})$ for this cubic phase, i.e., $1/3V \propto 1.64 + 0.005x$. Thus, migration of $x/2$ Al^{3+} from the 16d site to the x amount of Al^{3+} in the 8a site leads to a small increase in V. Rietveld refinement was performed (occupancy of Al/Mg was not refined because of a too small difference in their X-ray atomic scattering power), as shown in Fig. 4a–c. The V behavior per T is plotted in Fig. 4d. The refinements were stable and ended with relatively low R-factors (Table 2). Coordinates of atoms and main bond lengths are listed in Tables 3 and 4, respectively. Although the V for the sample sintered at 700 °C has a relatively large esd (effective standard deviation), it is clear that V increases with the calcination temperature, and thus, the concentration of anti-site disorder increases in the order of $T = 700$, 1000, 1300 °C. This V–T trend is in accordance with what has been observed by the in situ measurement on $MgAl_2O_4$ single crystals.[44]

The fact that the anti-site disorder increases with the temperature-rise in the $MgAl_2O_4:Mn^{4+}$ phosphors is contradictory to the observation that the FWHM decreases with the temperature-rise, since a higher disorder degree of lodcal coordination generally leads to larger FWHM of an electric dipole transition. Therefore, we presume that there exists another factor playing a more important role than the anti-site disorder which is affecting the FWHM of the $MgAl_2O_4:Mn^{4+}$ luminescence. It is noticed from Table 3 that at higher temperatures, the isotropic displacement parameter (B_{iso}) of all constituent atoms exhibits a clear decrease. In the spinel, the oxygen atoms are located at the (u,u,u) site; since Mn^{4+} dopants are bound to oxygen, the
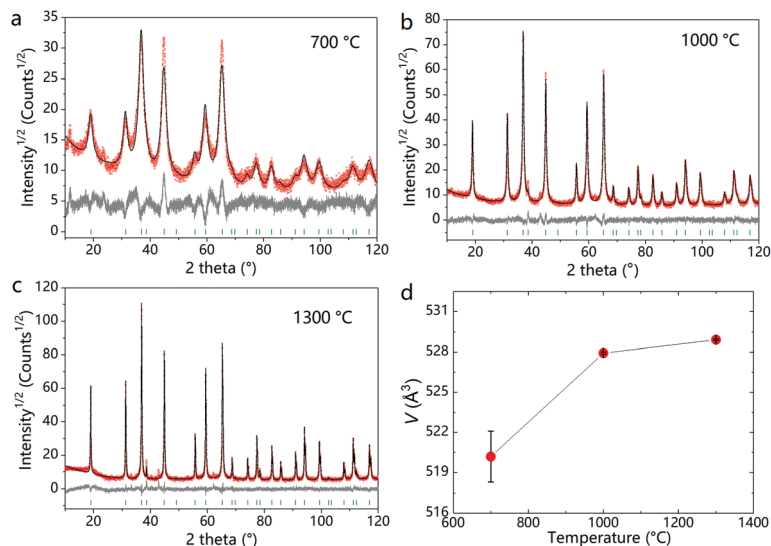
Fig. 4 Observed (red), calculated (black), and difference (gray) XRD profiles of the MgAl$_2$O$_4$:Mn^{4+} phosphors synthesized at temperatures of (a) 700 °C, (b) 1000 °C, and (c) 1300 °C refined by the Rietveld method. Bragg reflections are indicated by green ticks. (d) Cell volume behavior per T.

Table 2 Main parameters for the processing and refinement of MgAl$_2$O$_4$:Mn^{4+}

T, °C	Space group	Cell parameters (Å), cell volume (Å^3)	R_{wp}, R_p, R_{Brag}, χ^2
700	$Fd\bar{3}m$	$a = 8.0712$ (12), $V = 525.80$ (22)	14.08, 11.59, 5.26, 1.83
1000	$Fd\bar{3}m$	$a = 8.0853$ (5), $V = 528.55$ (10)	10.92, 8.10, 2.01, 1.36
1300	$Fd\bar{3}m$	$a = 8.08630$ (7), $V = 528.748$ (14)	12.15, 8.33, 1.62, 1.52

Table 4 Main bond lengths (Å) of MgAl$_2$O$_4$:Mn^{4+}

T = 700 °C			
Mg–O	1.826 (4)	Al–O^i	1.974 (4)
T = 1000 °C			
Mg–O	1.9006 (12)	Al–O^i	1.9385 (12)
T = 1300 °C			
Mg–O	1.9156 (10)	Al–O^i	1.9311 (10)

Symmetry codes: (i) $-x + 1$, $z + 1/4$, $y + 1/4$.

Table 3 Fractional atomic coordinates and isotropic displacement parameters (Å^2) of MgAl$_2$O$_4$:Mn^{4+}

Atom	X	y	z	B_{iso}	Occupation
T = 700 °C					
Mg	0.125	0.125	0.125	1.0 (7)	1
Al	0.5	0.5	0.5	1.0 (4)	1
O	0.2556 (5)	0.2556 (5)	0.2556 (5)	0.8 (6)	1
T = 1000 °C					
Mg	0.125	0.125	0.125	0.54 (17)	1
Al	0.5	0.5	0.5	0.66 (9)	1
O	0.26072 (15)	0.26072 (15)	0.26072 (15)	0.76 (13)	1
T = 1300 °C					
Mg	0.125	0.125	0.125	0.31 (6)	1
Al	0.5	0.5	0.5	0.47 (6)	1
O	0.26177 (12)	0.26177 (12)	0.26177 (12)	0.55 (7)	1

thermal effect on the B_{iso} parameter of the (u,u,u) site can account for the FWHM variation. The Stokes vibronic emissions of Mn^{4+} ^{2}E$_g$ → ^{4}A$_{2g}$ forbidden transition gain intensity from the ungerade vibrational modes including the asymmetric bending (ν_6, ν_4) and asymmetric stretching (ν_3) of the MnO$_6$ moieties. To verify the correlation between the decrease

of the B_{iso} parameter and the vibrational modes of the spinel lattice, we collected the Raman spectra in the spectral range 200–900 cm^{-1}, as shown in Fig. 5. Three relatively clear Raman modes are observed and marked accordingly.[45] When heated at 700 °C, the halo Raman modes with very weak intensity are seen, and it is difficult to identify the modes. When heated at 1000 °C, the E$_g$ Raman mode is noticeable, which becomes narrower in the sample heated at 1300 °C. Comparison of the Raman spectra collected for these three phosphors indicates that the structural rigidness gradually increased with the heating temperature. Thus, the decrease of the B_{iso} parameter of the oxygen atoms (of course, also the Al and Mg atoms) was verified by Raman measurement, besides the evidence from the Rietveld refinement of the XRD patterns. Such decrease of the B_{iso} parameter of consistent atoms leads to the restrain of the strength of phonon scattering and the strength of electron–phonon coupling, as well as the ordering of the ungerade vibrational modes (ν_6, ν_4, ν_3), which result in the decrease of observed PL FWHM of Mn^{4+} ^{2}E$_g$ → ^{4}A$_{2g}$ transition in MgAl$_2$O$_4$. Wang et al.[46] prepared MgAl$_2$O$_4$:Eu^{3+} by a solution combustion method with heating temperatures of 700–1200 °C, and they demonstrated that the Debye temperatures of the samples show a positive relationship with the calcination temperature. Thus, the decrease of the B_{iso} parameter of all atoms in the
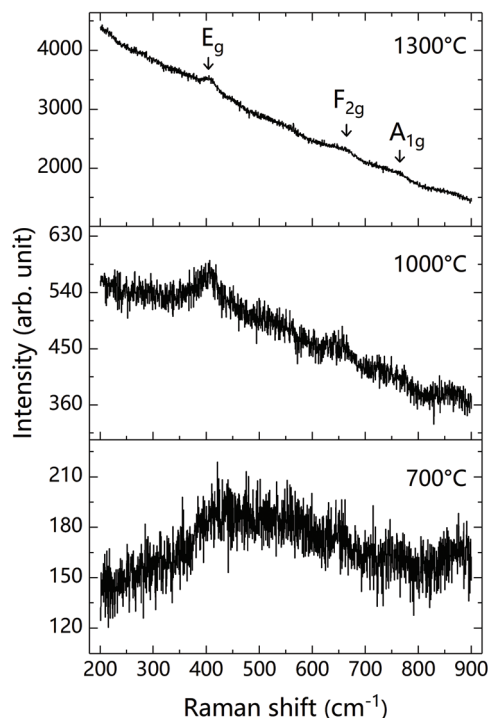
Fig. 5 Raman spectra recorded for the MgAl$_2$O$_4$:Mn^{4+} phosphors synthesized at temperatures of 700 °C, 1000 °C, and 1300 °C. The observed Raman modes are marked.

present MgAl$_2$O$_4$:Mn^{4+} phosphors can also be regarded as a dynamic improvement of structural rigidity.

3.3 Chemically induced order–disorder in the MgAl$_2$O$_4$:Mn^{4+} phosphor and its luminescence properties

Although the inhomogeneous broadening of the luminescence spectra of MgAl$_2$O$_4$:Mn^{4+} is mainly induced by the decrease of

the B_{iso} parameter of consistent atoms, the effect of the Mg–Al anti-site disorder cannot be fully neglected. As a proof of concept, we further prepare MgAl$_2$O$_4$:Mn^{4+} at a really high temperature (1550 °C for 6 h), but introduce Ga^{3+} with a larger ionic size to partially replace Al^{3+} as a way to chemically control the anti-site disorder degree of the spinel phosphor.

MgAl$_2$O$_4$ is the parent compound of the spinel group, compositions of which can be generalized as AB$_2$X$_4$. In a fully inverse spinel, 1/8th of the tetrahedral sites are filled with B^{3+} and 1/4th of the octahedral sites are filled with A^{2+} and 1/4th are filled with B^{3+}.[47] The relative distributions of the cations at these octahedral/tetrahedral sites are influenced by the ionic radius and electronegativity of the cations.[48] Thus, besides temperature, the anti-site disorder can be induced chemically. For example, MgGa$_2$O$_4$ has a larger degree of site inversion than MgAl$_2$O$_4$ due to the larger ionic size of Ga^{3+} than Al^{3+} (unit cells shown in Fig. 6a and b). Moreover, it has been demonstrated that a complete solid solution can form between MgAl$_2$O$_4$ and MgGa$_2$O$_4$ at 1550 °C.[49] We thus came up with the idea of preparing MgAl$_{2-x}$Ga$_x$O$_4$:Mn^{4+} solid solution phosphors to observe the FWHM evolution of the PL bands in response to the progressive anti-site disordering induced by the substitution of Al^{3+} by Ga^{3+}. XRD confirmed the formation of a single phase when x is equal to 0, 0.5 and 1.0 by comparing the measured pattern with those of MgAl$_2$O$_4$ (JCPDS no. 047-254) and MgAl$_{1.04}$Ga$_{0.96}$O$_4$ (JCPDS no. 04-007-2715) (as shown in Fig. 6c). As seen from Fig. 6e, the ZPL of Mn^{4+} ^{2}E$_g$ → ^{4}A$_{2g}$ transition is almost independent of crystal field strength but varies with the different nephelauxetic effects experienced by the Mn^{4+} 3d orbital. Thus, the PL bands (λ_{ex} = 440 nm) of the MgAl$_{2-x}$Ga$_x$O$_4$:Mn^{4+} phosphors were normalized at the respective peak emissions. Indeed, as seen from Fig. 6d, the PL band becomes broadened with the intensity of the longer wavelength emission getting enhanced as x changes from 0 to 1.0. Thus, using the chemically induced order–disorder in
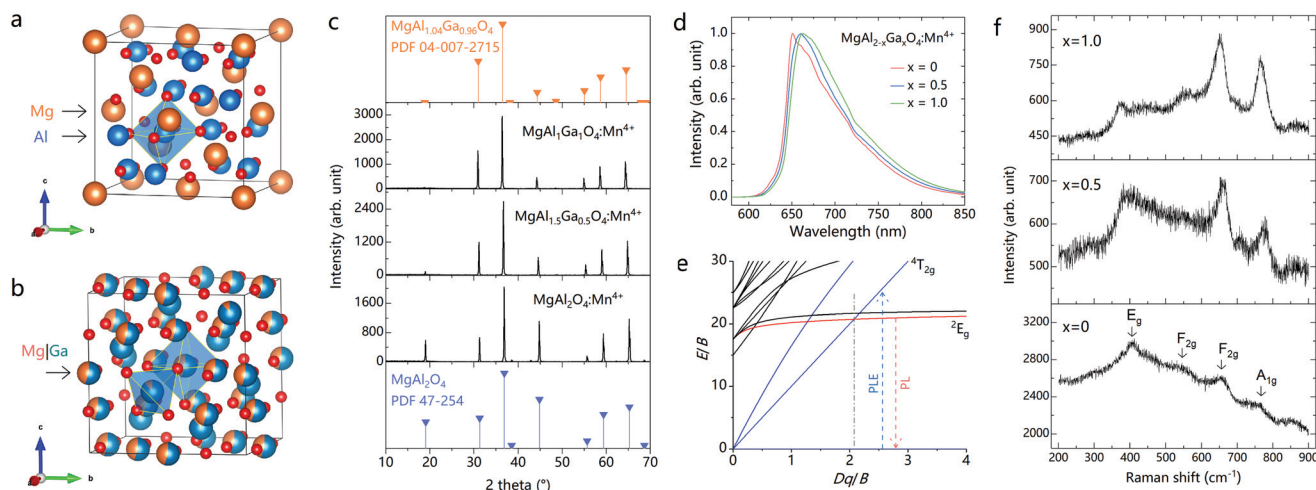

Fig. 6 (a) Unit cells of MgAl$_2$O$_4$ (ICSD_CollCode31373) and (b) unit cell of MgGa$_2$O$_4$ (ICSD_CollCode4806). Drawn with VESTA.[50] (c) XRD patterns and (d) PL spectra (λ_{ex} = 440 nm) of the MgAl$_{2-x}$Ga$_x$O$_4$:Mn^{4+} phosphors. (e) Tanabe–Sugano diagram for a d^3 ion. (f) Raman spectra of the MgAl$_{2-x}$Ga$_x$O$_4$:Mn^{4+} (x = 0, 0.5, 1.0) phosphors.

$MgAl_2O_4:Mn^{4+}$, the relationship between the large FWHM and the anti-site defect can be further verified. Since the preparation was conducted at a quite high temperature of 1550 °C, the Raman modes are clear (see the Raman spectrum recorded for the $x = 0$ sample in Fig. 6f) but relatively broad indicating the existence of an anti-site disorder in the synthetic spinel. With the introduction of Ga^{3+}, the F_{2g} and A_{1g} Raman modes get their intensity enhanced associated with a small shift, suggesting the incorporation of Ga^{3+} into the lattice and more importantly, the change in the dominating vibrational modes. Although the Mn^{4+} $^2E_g \rightarrow {}^4A_{2g}$ transition mainly couples with the ν_6 vibrational modes to gain intensity, the change in the dominating vibrational modes would reasonably change the relative intensity of the phonon sideband emissions. Thus, a varying FWHM of PL bands depending on the Al^{3+}-Ga^{3+} substitution induced anti-site disorder is observed.

3.4 Abnormal luminescence thermal quenching behavior of $MgAl_2O_4:Mn^{4+}$

The PL thermal quenching of the spinel phosphors was studied in the range of 100–470 K upon excitation with a 440 nm laser diode, as shown in Fig. 7. The quenching temperatures ($T_{50\%}$, the temperature at which the luminescence intensity drops to half of the initial value) are 250 K, 352 K, and 400 K for the phosphors heated at 700 °C, 1000 °C, and 1300 °C, respectively, which show a significant change with varying calcination temperature. Although $T_{50\%}$ may be overestimated since the PL may steadily decrease with temperature rise between 0 K and 100 K, it is clear that the $T_{50\%}$ of Mn^{4+}

luminescence of the spinel phosphors shows dependence on the calcination temperature of the samples: a higher calcination temperature results in a higher $T_{50\%}$ of the sample.

In a paper published by Senden *et al.*[51] and in our previous work,[52] the consistency between the $^4T_{2g}$ level and $T_{50\%}$ has been demonstrated. However, from the present observation, it is found that even with the same $^4T_{2g}$ level of Mn^{4+} in the $MgAl_2O_4$ spinel, $T_{50\%}$ can differ significantly from 250 K, 352 K, and 400 K. That is to say, $T_{50\%}$ practically depends also on the preparation history; key factors associated with the preparation history may include the crystallinity and anti-site disorder concentration. In order to explore the intrinsic thermal quenching temperature of Mn^{4+} luminescence in $MgAl_2O_4$, we thus try to prepare the $MgAl_2O_4:Mn^{4+}$ phosphor with high crystallinity. A molten salt method which provides an unstrained environment for crystal growth was employed (details of the molten salt synthesis of $MgAl_2O_4:Mn^{4+}$ are given in ESI†), and the product is a highly crystalline spinel with a noticeably distinguished tetragonal-bipyramid morphology (shown in Fig. 8d). A large portion of spinel particles is found to exhibit well-developed facets, indicating the growth under approximate equilibrium conditions. This morphology is quite different from those observed for the samples prepared by the co-precipitation method (Fig. 8a–c) which are large particles with a non-uniform size of 1–20 μm. The large particle size of the $MgAl_2O_4:Mn^{4+}$ phosphors prepared by the co-precipitation method is due to the formation of AlOOH (which is very glutinous and favorable for particle aggregation) in the precursor as well as a long period of aging.
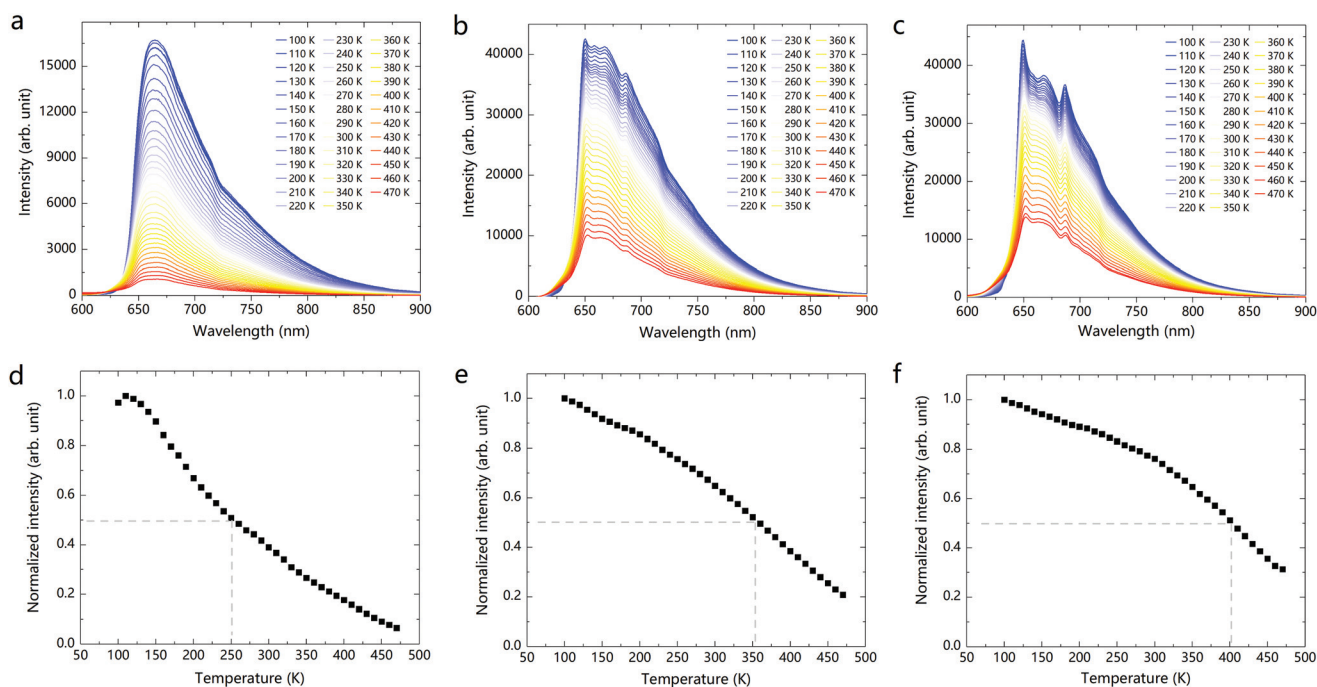

Fig. 7 Photoluminescence thermal quenching of the $MgAl_2O_4:Mn^{4+}$ phosphors prepared at temperatures of (a) 700 °C, (b) 1000 °C, (c) 1300 °C (λ_{ex} = 440 nm). The evolution of the integrated PL intensity (in the spectral range from 600 nm to 900 nm) against temperature is shown in (d), (e), and (f), respectively.
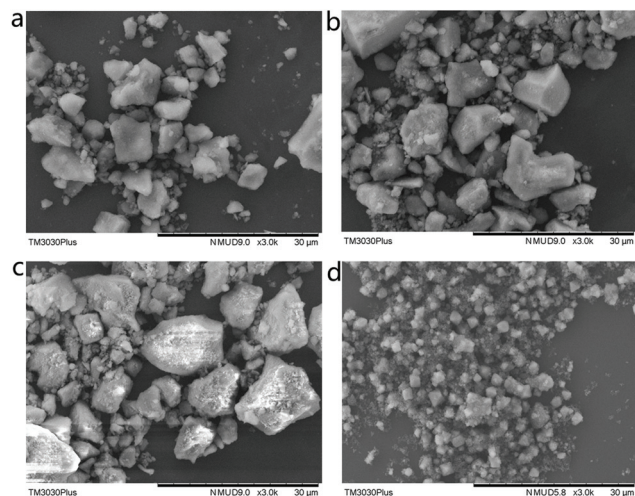
Fig. 8 SEM images of the MgAl$_2$O$_4$:Mn^{4+} phosphors prepared by the co-precipitation method followed by heating at: (a) 700 °C, (b) 1000 °C, and (c) 1300 °C. (d) shows the SEM image of MgAl$_2$O$_4$:Mn^{4+} prepared by the molten salt synthesis method.

The thermal quenching behavior (Fig. 9a and b) of the MgAl$_2$O$_4$:Mn^{4+} phosphor prepared by the molten salt method shows high similarity to that of the phosphor prepared by co-precipitation and heating at 1300 °C. $T_{50\%}$ estimated for this sample is around 390 K (Fig. 9c), which is very close to the value estimated in Fig. 7f; thus, the intrinsic $T_{50\%}$ for Mn^{4+} luminescence in MgAl$_2$O$_4$ is believed to be around 390–400 K. Among the four Mn^{4+}-doped aluminate phosphors emitting around 650 nm, this $T_{50\%}$ is lower than that of Sr$_4$Al$_{14}$O$_{25}$:Mn^{4+} (peaking emission 652 nm, $T_{50\%}$ 423 K),[53] but higher than that of Sr$_2$Al$_6$O$_{11}$:Mn^{4+} (peaking emission 652 nm, $T_{50\%}$

383 K)[8] and SrAl$_{12}$O$_{19}$:Mn^{4+} (peaking emission 655 nm, $T_{50\%}$ 300 K).[54]

Currently, the widely proposed thermal quenching mechanism for Mn^{4+} luminescence is thermal assisted crossover from the emitting ^2E_g state to the Franck–Condon shifted $^4T_{2g}$ and then non-radiative relaxation to the $^4A_{2g}$ state. According to the configuration coordinate model (Fig. 9d), if the $^4T_{2g}$ potential curve is right-shifted ($^4T_{2g}{}^*$) further offsetting the $^4A_{2g}$ level, the activation energy E_a of thermal crossover quenching decreases to a smaller E_a^*. The observed $T_{50\%}$ dependence on the calcination temperature can be regarded as the left-shift of the $^4T_{2g}$ potential curve with lower electron–phonon coupling at higher calcination temperature of the co-precipitated sample. The calcination of the co-precipitated precursor at 700, 1000, or 1300 °C results in the MgAl$_2$O$_4$:Mn^{4+} phosphor with varying Debye temperature, and thus, a varying electron–phonon coupling strength.

4 Conclusions

We prepared the MgAl$_2$O$_4$:Mn^{4+} red-emitting phosphors for blue LED pumped white lighting using a co-precipitation method followed by heating at different temperatures (700–1300 °C) in air. The phosphors exhibit ultrabroadband emission peaking at a short wavelength of 651 nm. The synthetic spinel accommodates the Mg^{2+} ↔ Al^{3+} anti-site disorder, leading to the ultrabroadband emission without fine structure between the ZPL and the phonon sideband emissions. The FWHM is dependent both on the calcination temperature and on the partial substitution of Al^{3+} by Ga^{3+}. The increase in heating temperature from 700 °C to 1300 °C leads to a
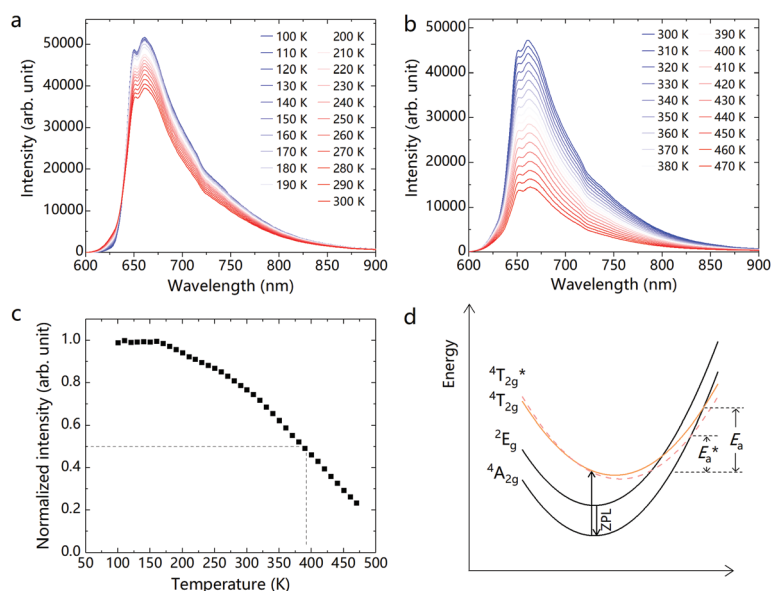

Fig. 9 Photoluminescence thermal quenching of the MgAl$_2$O$_4$:Mn^{4+} phosphor prepared by the molten salt synthesis method: (a) from 100 K to 300 K, (b) from 300 K to 470 K. The evolution of the integrated PL intensity (in the spectral range from 600 nm to 900 nm) against temperature is shown in (c). (d) The thermal assisted crossover model explaining thermal quenching and the $T_{50\%}$ dependence on the calcination temperature.

decrease in the anti-site disorder concentration, while the chemical substitution of Al^{3+} by Ga^{3+} results in an increase in the anti-site disorder concentration. By means of Rietveld refinement and Raman techniques, such variation of the PL FWHM has been found to be a sum effect of structural ordering (*i.e.*, isotropic displacement decrease of constituent atoms) and the Mg ↔ Al anti-site disorder. The phosphor heated at a higher calcination temperature exhibits a higher thermal quenching temperature $T_{50\%}$, which can be explained by the lower electron–phonon coupling in the configuration coordinate model. The intrinsic $T_{50\%}$ for Mn^{4+} luminescence in $MgAl_2O_4$ is believed to be around 390–400 K. The novel understanding of the ultrabroad emission peaking at 651 nm and the abnormal thermal quenching behavior provides new insights into developing high-performance Mn^{4+}-based red phosphors.

Conflicts of interest

There are no conflicts to declare.

Acknowledgements

References

1 Z. Xia and A. Meijerink, *Chem. Soc. Rev.*, 2017, **46**, 275–299.

2 H. F. Sijbom, R. Verstraete, J. J. Joos, D. Poelman and P. F. Smet, *Opt. Mater. Express*, 2017, **7**, 3332–3365.

3 Z. Zhou, N. Zhou, M. Xia, M. Yokoyama and H. T. Hintzen, *J. Mater. Chem. C*, 2016, **4**, 9143–9161.

4 E. Langenberg, E. Ferreiro-Vila, V. Leborán, A. O. Fumega, V. Pardo and F. Rivadulla, *APL Mater.*, 2016, **4**, 104815.

5 Y. Tanabe and S. Sugano, *J. Phys. Soc. Jpn.*, 1954, **9**, 766–779.

6 Y. D. Xu, D. Wang, L. Wang, N. Ding, M. Shi, J. G. Zhong and S. Qi, *J. Alloys Compd.*, 2013, **550**, 226–230.

7 M. Peng, X. Yin, P. A. Tanner, C. Liang, P. Li, Q. Zhang and J. Qiu, *J. Am. Ceram. Soc.*, 2013, **96**, 2870–2876.

8 T. Sasaki, J. Fukushima, Y. Hayashi and H. Takizawa, *J. Lumin.*, 2018, **194**, 446–451.

9 L. Wang, Y. Xu, D. Wang, R. Zhou, N. Ding, M. Shi, Y. Chen, Y. Jiang and Y. Wang, *Phys. Status Solidi A*, 2013, **210**, 1433–1437.

10 B. Wang, H. Lin, J. Xu, H. Chen and Y. Wang, *ACS Appl. Mater. Interfaces*, 2014, **6**, 22905–22913.

11 R. Cao, Q. Xiong, W. Luo, D. Wu, X. Fen and X. Yu, *Ceram. Int.*, 2015, **41**, 7191–7196.

12 J. Park, G. Kim and Y. J. Kim, *Ceram. Int.*, 2013, **39**, S623–S626.

13 R. Cao, M. Peng, E. Song and J. Qiu, *ECS J. Solid State Sci. Technol.*, 2012, **1**, R123–R126.

14 T. Murata, T. Tanoue, M. Iwasaki, K. Morinaga and T. Hase, *J. Lumin.*, 2005, **114**, 207–212.

15 R. Cao, K. N. Sharafudeen and J. Qiu, *Spectrochim. Acta, Part A*, 2014, **117**, 402–405.

16 B. Wang, H. Lin, F. Huang, J. Xu, H. Chen, Z. Lin and Y. Wang, *Chem. Mater.*, 2016, **28**, 3515–3524.

17 B. W. Nuryadin, A. Sawitri, E. C. S. Mahen and A. Y. Nuryantini, *J. Phys.: Conf. Ser.*, 2017, **812**, 12020.

18 M. Aoyama, Y. Amano, K. Inoue, S. Honda, S. Hashimoto and Y. Iwamoto, *J. Lumin.*, 2013, **136**, 411–414.

19 J. F. Donegan, T. J. Glynn, G. F. Imbusch and J. P. Remeika, *J. Lumin.*, 1986, **36**, 93–100.

20 T. Jansen, T. Jüstel, M. Kirm, S. Vielhauer, N. M. Khaidukov and V. N. Makhov, *J. Lumin.*, 2018, **198**, 314–319.

21 Y. Xu, L. Wang, B. Qu, D. Li, J. Lu and R. Zhou, *J. Am. Ceram. Soc.*, 2019, **102**, 2737–2744.

22 M. G. Brik, I. Sildos, M. Berkowski and A. Suchocki, *J. Phys.: Condens. Matter*, 2008, **21**, 25404.

23 A. M. Srivastava and M. G. Brik, *Opt. Mater.*, 2017, **63**, 207–212.

24 Q. Sun, S. Wang, B. Devakumar, L. Sun, J. Liang, X. Huang and Y. Wu, *J. Alloys Compd.*, 2019, **785**, 1198–1205.

25 A. M. Srivastava and M. G. Brik, *Opt. Mater.*, 2013, **35**, 1544–1548.

26 B. D. McNicol and G. T. Pott, *J. Lumin.*, 1973, **6**, 320–334.

27 W. Lü, W. Lv, Q. Zhao, M. Jiao, B. Shao and H. You, *Inorg. Chem.*, 2014, **53**, 11985–11990.

28 Y. Zhydachevskii, A. Suchocki, A. Pajączkowska, A. Kłos, A. Szysiak and A. Reszka, *Opt. Mater.*, 2013, **35**, 1664–1668.

29 J.-G. Li, T. Ikegami, J.-H. Lee, T. Mori and Y. Yajima, *J. Eur. Ceram. Soc.*, 2001, **21**, 139–148.

30 M. F. Zawrah, H. Hamaad and S. Meky, *Ceram. Int.*, 2007, **33**, 969–978.

31 *TOPAS V4.2: General profile and structure analysis software for powder diffraction data – User's Manual*, Bruker AXS, Karlsruhe, Germany.

32 H. Ji, J. Xu, K. Asami, J. Ueda, M. G. Brik and S. Tanabe, *J. Am. Ceram. Soc.*, 2019, **102**, 1316–1328.

33 B. Z. Malkin, *Mod. Probl. Condens. Matter Sci.*, 1987, **21**, 13–50, DOI: 10.1016/B978-0-444-87051-3.50008-0.

34 N. M. Avram and M. G. Brik, *Optical Properties of 3d-Ions in Crystals: Spectroscopy and Crystal Field Analysis*, 2013.

35 M. G. Brik and Y.-Y. Yeung, *J. Phys. Chem. Solids*, 2008, **69**, 2401–2410.

36 Y. Wakui, Y. J. Shan, K. Tezuka, H. Imoto and M. Ando, *Mater. Res. Bull.*, 2017, **90**, 51–58.

37 M. G. Brik, W. W. Beers, W. Cohen, S. A. Payne, N. J. Cherepy, M. Piasecki and A. M. Srivastava, *Opt. Mater.*, 2019, **91**, 338–343.

38 S. Adachi, *ECS J. Solid State Sci. Technol.*, 2020, **9**, 016001.

39 H. Ji, L. Wang, M. S. Molokeev, N. Hirosaki, R. Xie, Z. Huang, Z. Xia, O. M. ten Kate, L. Liu and V. V. Atuchin, *J. Mater. Chem. C*, 2016, **4**, 6855–6863.

40 H. Ji, L. Wang, M. S. Molokeev, N. Hirosaki, Z. Huang, Z. Xia, O. M. ten Kate, L. Liu and R. Xie, *J. Mater. Chem. C*, 2016, **4**, 2359–2366.

41 H. Ji, Z. Huang, Z. Xia, M. S. Molokeev, V. V. Atuchin, M. Fang and Y. Liu, *J. Phys. Chem. C*, 2015, **119**, 2038–2045.

42 H. Ji, Z. Huang, Z. Xia, M. S. Molokeev, V. V. Atuchin and S. Huang, *Inorg. Chem.*, 2014, **53**, 11119–11124.

43 J. A. Ball, M. Pirzada, R. W. Grimes, M. O. Zacate, D. W. Price and B. P. Uberuaga, *J. Phys.: Condens. Matter*, 2005, **17**, 7621–7631.

44 T. Yamanaka and Y. Takéuchi, *Z. Kristallogr. – Cryst. Mater.*, 1983, **165**, 65–78.

45 V. D'Ippolito, G. B. Andreozzi, D. Bersani and P. P. Lottici, *J. Raman Spectrosc.*, 2015, **46**, 1255–1264.

46 Z. Wang, S. Jiao, Y. Xu, Q. Zhang, Y. Chen, G. Pang and S. Feng, *J. Lumin.*, 2019, **211**, 108–113.

47 K. E. Sickafus, J. M. Wills and N. W. Grimes, *J. Am. Ceram. Soc.*, 1999, **82**, 3279–3292.

48 C. Jagadeeshwaran, K. Madhan and R. Murugaraj, *J. Mater. Sci.: Mater. Electron.*, 2018, **29**, 18923–18934.

49 R. Stalder and K.-H. Nitsch, *J. Am. Ceram. Soc.*, 1997, **80**, 258–260.

50 K. Momma and F. Izumi, *J. Appl. Crystallogr.*, 2011, **44**, 1272–1276.

51 T. Senden, R. J. A. van Dijk-Moes and A. Meijerink, *Light: Sci. Appl.*, 2018, **7**, 8.

52 H. Ji, J. Ueda, M. Brik, M. H. Du, D. Chen and S. Tanabe, *Phys. Chem. Chem. Phys.*, 2019, **21**, 25108–25117.

53 M. Peng, X. Yin, P. A. Tanner, M. G. Brik and P. Li, *Chem. Mater.*, 2015, **27**, 2938–2945.

54 X. Wang, P. Li, M. G. Brik, X. Li, L. Li and M. Peng, *J. Lumin.*, 2019, **206**, 84–90.